Modeling of Globular Equiaxed Solidification with a Two-Phase Approach

ANDREAS LUDWIG and MENGHUAI WU

A two-phase volume averaging model for globular equiaxed solidification is presented. Treating both liquid and solid (disperse grains) as separated but highly coupled interpenetrating continua, we have solved the conservation equations for mass, momentum, species mass fraction, and enthalpy for both phases. We also consider the conservation of grain density. Exchange or source terms take into account interactions between the melt and the solid, such as mass transfer (solidification and melting), friction and drag, solute redistribution, release of latent heat, and nucleation. An ingot casting with a near globular equiaxed solidification alloy (A1-4 wt pct Cu) is simulated. Results including grain evolution, melt convection, sedimentation, solute transport, and macrosegregation formation are obtained. The mechanisms producing these results are discussed in detail.

I. INTRODUCTION

MODELING of solidification and grain formation is a multiphase and multiscale problem. Solidification sequence, shrinkage cavity formation, macrostructure, and macrosegregation formations are governed by mass, momentum, heat, and species transport phenomena on the system scale, while modeling of the solidification morphology and microstructure requires understanding of nucleation, growth kinetics, and species redistribution on interfacial and even atomic scale. Great efforts and progress have been made to model these phenomena with multiscale coupling.[1,2] The most promising model was the multiphase volume-averaging approach developed by Beckermann's group.[2–8] They treated the liquid and the solid as separated but highly coupled and interpenetrating continua, and they established and solved the transport equations for both liquid and solid simultaneously, thereby permitting a rigorous description of the liquid convection and the solid movement, mass transfer between solid and liquid (solidification and remelting), solute partitioning, and many other microscopic phenomena. However, this pioneering model involves many uncertainties,[9,10] for example, the lack of a realistic nucleation model, detailed volumetric heat and mass transfer coefficients (or thermal and solutal diffusion lengths), correct stereological formulations for interfacial area concentration, *etc.* A good deal of additional research is needed before the advantages of the model may be fully exploited.[2,6,11]

Globular equiaxed solidification has an easy-to-define morphology. The solidified grains can be simplified as spheres. The grain size can be expressed with a volume-averaged diameter, avoiding the uncertainties mentioned previously on modeling the interfacial area concentration and the complexity for handling of the interdendritic melt in dendritic solidification. Modeling globular equiaxed solidification also has wide engineering application prospects. Many high-performance materials require fine globular grains, *e.g.*, the newly developed thixoforming process requires the prematerial being made with spherical grains.[12,13]

This article presents a two-phase volume averaging model, which is particularly valid for globular solidification alloys.[14,15] The classical nucleation law and growth kinetics[1,16,17] are implemented in the model. We have simulated a benchmark ingot casting (A1-4 wt pct Cu) emphasizing microscopic modeling, *i.e.*, the definition of different source, interaction, and exchange terms for the macroconservation equations.

Although the theory and the solution procedure apply to the multiphase and multicomponent system in general, the macroconservation equations described subsequently specialize on two phases (liquid l and solid s) and two components (Al and Cu in Al-4 wt pct Cu alloy) for clarity and simplicity.

II. MODEL DESCRIPTION

A. *Conservation Equations*

We considered a single-phase globular solidification. The volume fraction of liquid, denoted by f_l, and the volume fraction of solid, denoted by f_s, are assumed to be continuous functions of space and time. Their sum is equal to one: $f_l + f_s = 1$.

We formulated conservation equations of mass, momentum, species, and enthalpy for both phases, liquid and solid, taking into account microscopic phenomena caused by solidification by including different exchange terms. Section II-C gives details of these exchange terms.

$$\frac{\partial}{\partial t}(f_l \rho_l) + \nabla \cdot (f_l \rho_l \mathbf{u}_l) = M_{sl} \qquad [1]$$

$$\frac{\partial}{\partial t}(f_s \rho_s) + \nabla \cdot (f_s \rho_s \mathbf{u}_s) = M_{ls} \qquad [2]$$

are the conservation equations of mass. Here, M_{ls} is the mass transfer rate from liquid to solid, and M_{sl} $(= -M_{ls})$ that from solid to liquid. The unit of M_{ls} is kg/m^3/s. A positive M_{ls} characterizes solidification; otherwise, it characterizes melting. The terms ρ_l and ρ_s are the densities and $\mathbf{u}_l$ and $\mathbf{u}_s$ are the velocities of the liquid and solid phases. Navier–Stokes equations describe the momentum conservation:

ANDREAS LUDWIG and MENGHUAI WU, Senior Scientists, are with the Foundry Institute of Aachen, Aachen University (RWTH), D-52072 Aachen, Germany. Contact e-mail: ludwig@gi.rwth-aachen.de

Manuscript submitted March 5, 2002.

$$\frac{\partial}{\partial t}(f_l\rho_l\mathbf{u}_l) + \nabla\cdot(f_l\rho_l\mathbf{u}_l\otimes\mathbf{u}_l) = -f_l\nabla p + \nabla\cdot\bar{\bar{\tau}}_l + f_l\rho_l\mathbf{g} + \mathbf{U}_{sl} \quad [3]$$

$$\frac{\partial}{\partial t}(f_s\rho_s\mathbf{u}_s) + \nabla\cdot(f_s\rho_s\mathbf{u}_s\otimes\mathbf{u}_s) = -f_s\nabla p + \nabla\cdot\bar{\bar{\tau}}_s + f_s\rho_s\mathbf{g} + \mathbf{U}_{ls} \quad [4]$$

Here, $\mathbf{u}_l = (u_l, v_l)^T$ and $\mathbf{u}_s = (u_s, v_s)^T$ are velocity vectors of the liquid and solid phases. $\mathbf{U}_{ls}$ $(= -\mathbf{U}_{sl})$ is the momentum exchange rate between both phases. The unit of $\mathbf{U}_{ls}$ is kg/m^2/s^2. The term p is the pressure and $\mathbf{g}$ is the gravity. $\otimes$ is the dyadic product.

$$\bar{\bar{\tau}}_l = \mu_l f_l(\nabla\cdot\mathbf{u}_l + (\nabla\cdot\mathbf{u}_l)^T) \text{ and } \bar{\bar{\tau}}_s = \mu_s f_s(\nabla\cdot\mathbf{u}_s + (\nabla\cdot\mathbf{u}_s)^T) \quad [5]$$

show the stress-strain tensors, $\bar{\bar{\tau}}_l$ and $\bar{\bar{\tau}}_s$, where μ_l and μ_s represent the viscosity of the liquid and the solid phases, respectively. For further details on the definition of the viscosity of the solid, see Section II–B. We do not include turbulent terms (Reynolds stresses) in the recent model. It is valid for a system with laminar flow, *i.e*, the system Reynolds number $\mathrm{Re} = L\cdot\mathbf{u}_l\cdot\rho_l/\mu_l$ must be less or equal to 2100.[27] The term L is the character size of the fluid domain (casting size). Species conservation is

$$\frac{\partial}{\partial t}(f_l\rho_l c_l) + \nabla\cdot(f_l\rho_l\mathbf{u}_l c_l) = \nabla\cdot(f_l\rho_l D_l\nabla c_l) + C_{sl} \quad [6]$$

$$\frac{\partial}{\partial t}(f_s\rho_s c_s) + \nabla\cdot(f_s\rho_s\mathbf{u}_s c_s) = \nabla\cdot(f_s\rho_s D_s\nabla c_s) + C_{ls} \quad [7]$$

where C_{ls} $(= -C_{sl})$ is the species exchange rate between both phases. As c_l and c_s represent mass fractions, they are dimensionless. Thus C_{ls} has the unit of kg/m^3/s. The terms D_l and D_s are the diffusion coefficients of the solute in the liquid and solid phases. The enthalpy conservation equations are

$$\frac{\partial}{\partial t}(f_l\rho_l h_l) + \nabla\cdot(f_l\rho_l\mathbf{u}_l h_l) = \nabla\cdot(f_l k_l\nabla\cdot T_l) + Q_{sl} \quad [8]$$

$$\frac{\partial}{\partial t}(f_s\rho_s h_s) + \nabla\cdot(f_s\rho_s\mathbf{u}_s h_s) = \nabla\cdot(f_s k_s\nabla\cdot T_s) + Q_{ls} \quad [9]$$

where Q_{ls} $(= -Q_{sl})$ is the energy exchange rate between both phases. The unit of h_l and h_s is J/kg. Thus, Q_{ls} has the unit of J/m^3/s. The terms k_l and k_s are the heat conductivities of the liquid and solid phases. The relationship between the enthalpy h_l (or h_s) and the temperature T_l (or T_s) is determined *via*

$$h_l = \int_{T_{\mathrm{ref}}}^{T_l} c_{p(l)}\,dT + h_l^{\mathrm{ref}} \text{ and } h_s = \int_{T_{\mathrm{ref}}}^{T_s} c_{p(s)}\,dT + h_s^{\mathrm{ref}} \quad [10]$$

where $c_{p(l)}$ and $c_{p(s)}$ are the specific heat capacities of the liquid and solid phases, and h_l^{ref} and h_s^{ref} are the enthalpies at the reference temperature T_{ref}. In this article, we chose T_{ref} to be 273 K for both phases.

In addition to the conservation equations of mass, momentum, species, and enthalpy for both liquid and solid, the conservation of grains is

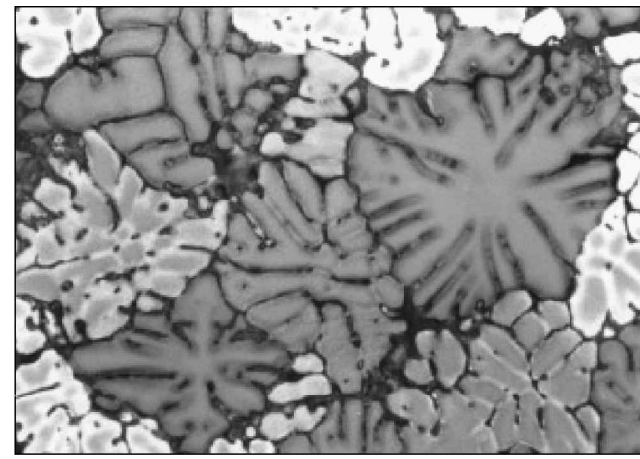

Fig. 1—Typical micrograph of an Al-4 wt pct Cu with some ppm Ti as the grain refiner.

$$\frac{\partial}{\partial t}n + \nabla\cdot(\mathbf{u}_s n) = N \quad [11]$$

Here, n is the grain density and N the grain production (nucleation rate). The unit of n is m^{-3}. Thus, N has the unit of m^{-3} s^{-1}. As stated in Section II–C–5, N is positive with nucleation and negative with grain dissolution (total remelting).

B. *Auxiliary Quantities*

The following auxiliary quantities are used: (1) mixed concentration, c_{mix}; (2) average grain diameter, d_s; and (3) viscosity of the solid phase, μ_s. The mixed concentration is

$$c_{\mathrm{mix}} = \frac{c_l\cdot\rho_l\cdot f_l + c_s\cdot\rho_s\cdot f_s}{\rho_l\cdot f_l + \rho_s\cdot f_s} \quad [12]$$

To estimate the average grain diameter, we assume the morphology of the growing grains to be almost spherical, allowing the volume fraction of solid to be related to the grain density and the average grain volume by

$$f_s = n\cdot\frac{4\pi}{3}(d_s/2)^3 \quad [13]$$

The assumption of almost spherical grains restricts the validity of the present model to globular equiaxed solidifying alloys only. Figure 1 shows the microstructure of an Al-4 wt pct Cu alloy containing small amounts of Ti as the grain refiner (in the parts per million range). Such alloys are supposed to solidify with almost globular equiaxed, rather than distinct dendritic grains. We thus keep the model simple and avoid the introduction of different shape functions, interfacial area,[9,10,11] and further model complication.

As mentioned previously, the momentum of the solid phase is also treated like that of a fluid. Hence, the solution of the corresponding conservation equation requires the definition of a viscosity of the solid phase. This viscosity may be caused by collisions between individual rigid grains. It should increase with increasing solid volume fraction and crystal size because of stronger crystal interactions. Ishii and Zuber[18] found for the viscosity of a solid/liquid mixture

$$\mu_{\mathrm{mix}} = \mu_l\cdot(1 - f_s/f_s^c)^{-2.5\cdot f_s^c} \quad [14]$$

with f_s^c representing a critical solid volume fraction above which the equiaxed crystals merge to form a rigid solid structure. Assuming the validity of a mixing rule for viscosity,[3] $\mu_{\text{mix}} = f_l \mu_l + f_s \mu_s$, Eq.[14] can be used to derive an expression for the viscosity of the solid phase

$$\mu_s = \frac{\mu_l}{f} \cdot \left((1 - f_s/f_s^c)^{-2.5 \cdot f_s^c} - (1 - f_s) \right) \qquad [15]$$

We applied this approach in the present model. Like the literature[4,5,6] we assume that f_s^c is the packing limit $f_s^c = 0.637$. For $f_s > f_s^c$, μ_s is infinitely large. This forces the macroscopic velocity gradients in the solid to vanish. For example, if the rigid solid structure is attached to a wall, the solid velocity will then be uniformly equal to the velocity of the wall due to the nonslip condition.

C. *Exchange Terms*

The exchange of momentum, species, or enthalpy between the liquid and the solid $\mathbf{U}_{ls}$, C_{ls}, and Q_{ls}, can either be caused by a mechanical or a diffusional interaction (index: d) or by a phase change (index:p)[3].

$$\mathbf{U}_{ls} = \mathbf{U}_{ls}^d + \mathbf{U}_{ls}^p \qquad [16a]$$

$$C_{ls} = C_{ls}^d + C_{ls}^p \qquad [16b]$$

$$Q_{ls} = Q_{ls}^d + Q_{ls}^p \qquad [16c]$$

Mechanical interactions between the liquid and solid lead to friction and drag modeled by $\mathbf{U}_{ls}^d$ and to the introduction of heat transfer between l and s modeled in Q_{ls}^d. Diffusional interaction taking into account diffusional fluxes from interface areas into the bulk of a phase, especially for species and enthalpy,[3] can be modeled in C_{ls}^d and Q_{ls}^d. However, here we do not take into account the contribution of C_{ls}^d. In all cases, it yields $\mathbf{U}_{sl}^d = -\mathbf{U}_{ls}^d$, $C_{sl}^d = -C_{ls}^d$, and $Q_{sl}^d = -Q_s^d$.

The contributions due to phase change can be modeled as[3]

$$\mathbf{U}_{ls}^p = \mathbf{u}^* \cdot M_{ls} \qquad [17a]$$

$$C_{ls}^p = \mathrm{c}^* \cdot M_{ls} \qquad [17b]$$

$$Q_{ls}^p = \mathrm{h}^* \cdot M_{ls} \qquad [17c]$$

where $\mathbf{u}^*$, c^*, and h^* are average values of momentum, species, and enthalpy at the solid/liquid interface. The meaning of these terms is explained in sections II-C2 through II-C4. $M_{sl} = -M_{ls}$ shows that the conditions $\mathbf{U}_{sl}^p = -\mathbf{U}_{ls}^p$, $C_{sl}^p = -C_{ls}^p$, and $Q_{sl}^p = -Q_s^p$ are automatically fulfilled, if $\mathbf{u}^*$, $\mathbf{c}^*$ and h^* are taken to be equal for both the solid to liquid and the liquid to solid transitions.

1. *Mass transfer*

Solving Eqs. [1] through [11] gives the average temperature of a volume element, $T(=T_l = T_s$, as subsequently discussed), and the average species mass fraction in the liquid, c_l. It is now assumed that T is also present directly at the solid/liquid interface (uniform temperature distribution within a volume element) and that thermodynamic equilibrium yields. Therefore, the average species mass fraction (concentration) in the liquid at the interface is $c_l^* = (T - T_f)/m$, where T_f is the melting point of the solvent and m is the slope of the liquidus line taken from the phase diagram. Due to the solute enrichment around the growing solid phase, this species mass fraction is generally higher than the average species mass fraction within the control volume, c_l. The difference between c_l^* and c_l is defined as the driving force for phase change. This driving force will cause the solid/liquid interface areas of all grains within the volume element, $n \cdot (\pi d_s^2)$, to grow. While solidification proceeds, the grains impinge. Therefore, the total grain surface has to be corrected by an Avrami factor $(1 - f_s)$. The mass transfer rate M_{ls} is thus

$$M_{ls} = g_\alpha \cdot \left(\frac{T - T_f}{m} - \mathrm{c}_l \right) \cdot (n \cdot \pi d_s^2) \cdot \rho_s \cdot (1 - f_s) \qquad [18]$$

introducing the empirical constant g_α. The unit of g_α is m/s; ρ_s is used as an additional factor in order to change from volume to mass-transfer rate.

The suggested formulation treats solidification and melting symmetrically. The advantage of this approach is its simplicity, which, by changing the value of g_α, may help to investigate the necessary precision of a mass-transfer model (dendrite growth model, *etc.*) regarding the impact on the solidification process, grain formation, and the final macrosegregation pattern.

2. *Momentum transfer*

The choice of an adequate model for the mechanical momentum exchange between moving grains and the flowing melt is the subject of ongoing scientific interest.[19] The mechanical momentum exchange between a primary fluid q and a secondary fluid p is described by $\mathbf{U}_{pq}^d = K_{pq} (\mathbf{u}_p - \mathbf{u}_q)$. K_{pq} $(= K_{qp})$ is the interphase momentum exchange coefficient. In fluid/fluid flows, the secondary phase presumably forms droplets or bubbles with diameter d_p. This has an impact on how each of the fluids is assigned to a particular phase. For example, in flows where there are unequal amounts of two fluids, the predominant fluid should be modeled as the primary fluid, since the sparser fluid is more likely to form droplets or bubbles. Empirical expressions for K_{pq} for fluid/fluid flows are given in References 20 through 22.

In fluid/solid flows, the solid phase is assumed to consist of particles with diameter d_p. In this case, the fluid phase should be modeled as the primary phase. Depending on the special configuration of the fluid/solid mixture, several authors have derived models for the determination of K_{pq}.[22–27] The most general model, valid for a solid fraction from zero up to 0.7, is the classical model of Kozeny–Carman.[27] For a resting solid behaving like a porous medium, the most general model is that of Blake–Kozeny.[27] For most of the fluid/solid flow models, the momentum exchange coefficient is as follows:

$$K_{pq} = -f_q^2 \frac{\mu_q}{K} = -18 f_q^2 \frac{\mu_q f_p C_\varepsilon}{d_p^2} \qquad [19]$$

Here, the equivalence of the porous medium and submerged object approaches is used.[19] The term K represents the overall permeability (porous medium approach) and C_ε the settling ratio (submerged object approach). In our model, we used that of Kozeny–Carman for $f_s \leq f_s^c$ and Blake–Kozeny for $f_s \geq f_s^c$. We have thus applied

$$K_{sl} = -18 f_l^2 \frac{\mu_l f_s C_\varepsilon}{d^2} \text{ for } f_s \le f_s^c \quad \text{with } C_\varepsilon = 10 \frac{f_s}{f_l^3}$$
$$= -f_l^2 \frac{\mu_l}{K} \quad \text{for } f_s > f_s^c \quad \text{with } K = K_0 \frac{f_l^3}{f_s^2} \qquad [20]$$

To obtain continuous transition, we chose the empirical parameter K_0 to be $K_0 = d_s^2 / 180$ at $f_s = f_s^c$, which was then kept constant for $f_s > f_s^c$. Equation [20] is also based on the assumption of laminar flow. Here, the Reynolds number of the flow in the two-phase system is defined as $\mathrm{Re} = d_s \cdot \rho_l \cdot f_l \cdot \Delta\mathbf{u}/(\mu_l \cdot f_s)$,[27] where $\Delta\mathbf{u} = |\mathbf{u}_l - \mathbf{u}_s|$. For laminar flow, Re should be less than or equal to 10. The following case study has demonstrated that the relative velocity between the two phases is very small ($\Delta\mathbf{u} \le 1$ mm/s), so that Re is in order of $10^{-2} \sim 1$.

In order to evaluate the momentum exchange rate caused by the phase change, $\mathbf{U}_{ls}^p$, we considered the following. During solidification, a mass per unit volume and time of M_{ls} is taken away from the liquid. This mass has a momentum (per unit mass and time) of $\mathbf{u}_l \cdot M_{ls}$. On the other hand, we added the same amount of momentum to the solid. Referring to Eq. [17a], we thus have $\mathbf{U}_{ls}^p = \mathbf{u}^* \cdot M_{ls}$, with $\mathbf{u}^* = \mathbf{u}_l$ for solidification. By analogy, we have $\mathbf{U}_{ls}^p = \mathbf{u}^* \cdot M_{ls}$ with $\mathbf{u}^* = \mathbf{u}_s$ for melting.

3. *Solute redistribution*

In our article, we assume that the diffusional exchange of solute between the liquid and the solid is negligible, $C_{ls}^d \equiv 0$ (no effect of back diffusion on solute redistribution). The solute exchange caused by the phase change, C_{ls}^p, is modeled as follows. During solidification, the solute mass per unit volume and time, which would be transferred from the liquid to the solid without solute partitioning, is $c_l \cdot M_{ls}$. However, due to the existence of solute partitioning, the solid can only accept $k \cdot c_l \cdot M_{ls}$. Referring to Eq. [17b], we have therefore $C_{ls}^p = c^* \cdot M_{ls}$, with $c^* = k \cdot c_l$ for solidification.

During melting, the solute mass per unit volume and time transferred from the solid to the liquid is $c_s \cdot M_{ls}$. Now the solute mass is accepted from the liquid. Referring to Eq. [17b], we thus have $C_{sl}^p = c^* \cdot M_{ls}$, with $c^* = c_s$ for melting. Note that the concentration of the solid at the solid/liquid interface is $k \cdot c_l$. Due to microsegregation profiles within the solid (which are not modeled explicitly in this article), this value differs from the average concentration of the solid, c_s. Thus, generally, $c_s \neq k \cdot c_l$ holds, explaining the difference in C_{ls}^p for solidification and melting.

4. *Enthalpy exchange*

We solve the energy conservation equations, Eqs. [8] and [9], separately for both liquid and solid phases. The solidification model, however, is based on the precondition of thermal equilibrium, *i.e.*, $T_s = T_l$. To satisfy this precondition, the diffusional heat exchange coefficient H^* in the enthalpy exchange term $Q_{ls}^d = H^* (T_l - T_s)$ should be chosen to be as large as possible, but too large of an H^* will overwhelm the contribution of other terms in the energy conservation and cause the divergence of the numerical simulation. In this study, test simulations were carried out, and a suitably large value for H^* (10^9 W/m^2/K) is obtained. With this parameter, the precondition of thermal equilibrium is maintained and the numerical calculation results are stable.

The release of the latent heat, *i.e.*, the enthalpy exchange caused by phase change, is described as follows. We assume an initial condition of $T_l = T_s$. The enthalpy of the liquid h_l and the solid h_s are calculated *via* Eq. [10]. The enthalpy difference between the liquid and solid ($h_l - h_s$) defines the latent heat Δh_f. Physically, this heat is released at the solid/liquid interface. However, as we do not resolve the solid/liquid interface explicitly, the latent heat is considered in the volume element as average quantity. During solidification, the energy per volume and time given by the liquid is $Q_{ls}^p = h_l \cdot M_{ls}$. Referring to Eq. [17c], we have $Q_{ls}^p = h^* \cdot M_{ls}$ with $h^* = h_l$. However, only the amount of $h_s \cdot M_{ls}$ from $h_l \cdot M_{ls}$, which is given by the liquid, is added to the solid phase. The energy difference $(h_l - h_s) \cdot M_{ls}$, *i.e.*, the part due to the latent heat, will be added to the liquid or the solid phase in the following way. If the local volume fraction solid is less than 0.5, the latent heat is added to the liquid phase; otherwise, it is added to the solid phase. This manipulation would violate the thermal equilibrium precondition of $T_l = T_s$. With the diffusional heat exchange between the phases, the difference of T_l and T_s is leveled out immediately.

During melting, the enthalpy per unit volume and time transferred from the solid to the liquid is $h_s \cdot M_{sl}$. Thus, referring to Eq. [17c], we have $Q_{ls}^p = h^* \cdot M_{ls}$, with $h^* = h_s$ for melting. As an analogue to solidification, the heat for remelting is modeled.

5. *Nucleation*

Solidification can only occur if active nuclei exist in the melt. To describe the nucleation process in the presence of melt convection and grain movement, we employed the pragmatic approach originally developed by Oldfield[28] in which the heterogeneous nucleation phenomenon is understood[1,17] to occur at different classes of nucleation sites. Each class is activated at a particular undercooling, ΔT. In general, these classes move with melt convection and a sophisticated nucleation description should also model the movement of each individual class and the impact of this movement on the class distribution. However, this would be far beyond the scope of this article. Although it may not be physically correct, we assume that the different classes of nucleation sites are stationary and do not move with the melt.

Oldfield suggested a continuous rather than a discrete distribution of nucleation sites, $dn/d(\Delta T)$. He used a Gaussian distribution

$$\frac{dn}{d(\Delta T)} = \frac{n_{\max}}{\sqrt{2\pi} \cdot \Delta T_\sigma} \cdot e^{\frac{1}{2}\left(\frac{\Delta T - \Delta T_N}{\Delta T_\sigma}\right)^2} \qquad [21]$$

Here, $n_{\max}$ is the maximum grain density, ΔT_N the undercooling at which the distribution has its maximum, and ΔT_σ the Gaussian distribution width. In our model, we assume that $n_{\max}$, ΔT_N, and ΔT_σ are constants, which do not depend on temperature or solute concentration of the melt. If the undercooling at a certain volume element increases by $d(\Delta T)$, the number of grains in this volume increases by $dn = dn/_{d(\Delta T)} \cdot d(\Delta T)$ as long as the corresponding part of the distribution $dn/_{d(\Delta T)}$ still represents active nucleation sites. The question whether they do is related to the question whether the volume element has ever had the corresponding undercooling before. This statement is only true because of the assumption that the different classes of nucleation sites do not move. The maximum undercooling ever achieved, $\Delta T_{\max}$, is stored for each volume element and nucleation is considered only if $\Delta T > \Delta T_{\max}$. Of course, $\Delta T_{\max}$ is then

updated. As for binary alloys, undercooling is $\Delta T = T_f + m \cdot c_l - T$, where ΔT may alter due to the change of T or c_l or both. In order to apply Oldfield's model in the grain transport equation (Eq. [11]), N is defined as $\frac{dn}{d(\Delta T)} \cdot \frac{d(\Delta T)}{dt}$. Nucleation is assumed to occur in a partly solidified volume element, and therefore, Eq. [21] is multiplied by f_l to give the proper source term for Eq. [11].

During melting, the undercooling is negative ($M_{ls} < 0$). If this occurs, a zero source term in Eq. [11] ($N = 0$) is assumed until the solid volume fraction drops below 0.01 pct. Then, a negative nucleation rate is calculated similar to the previous description of the calculation of the dissolution rate. This decreases n toward zero.

Our nucleation model may also be adapted to describe the formation of small equiaxed grains on the mold wall by choosing an adequate set of parameters $n_{\max}$, ΔT_N and ΔT_σ for the volume elements adjacent to the mold, as suggested by Rappaz.[17]

D. *Numerical Implementation*

The solution procedure is shown in Figure 2. The conservation equations (Eqs. [1] through [11]) are numerically solved by using the fully implicit, control-volume-based CFD software FLUENT* (version 4.6.2). For each time-step, up to 60 (normally 20 to 40) iterations are necessary to decrease the normalized residual of h_l and h_s below the convergence limit of 10^{-6} and $\mathbf{u}_l$, $\mathbf{u}_s$, c_l, c_s, f_s, p, and n below 10^{-4}. On each iteration, the mass-transfer rate M_{ls} and the auxiliary terms d_s and c_{mix} are actualized first. Then, the exchange and source terms $\mathbf{U}_{ls}^d$, $\mathbf{U}_{ls}^p$, Q_{ls}^d, Q_{ls}^p, C_{ls}^d, C_{ls}^p, and N are calculated in corresponding user defined subroutines. Finally, the conservation equations of momenta, masses, enthalpies, and species are solved in the given order. If for one of the 11 quantities listed previously convergence is not achieved, and additional iteration follows. Both liquid and solid share a single pressure field p solved by using an extended SIMPLE algorithm.[29] The pressure correction equation is obtained from the sum of the normalized mass continuity equations (Eqs. [1] and [2]). The dependent thermal physical properties are updated before the next iteration is carried out.

*FLUENT is a trademark of Fluent, Inc., USA.

The mesh (or grid) density can impact the calculation accuracy, especially near the wall regions. Referring to the boundary-layer theory,[30] the mesh adjacent to the wall should obey

$$\Delta\delta \cdot \sqrt{\frac{\rho_l \cdot \mathbf{u}_l^\infty}{\mu_l \cdot \tilde{y}}} \leq 1 \qquad [22]$$

where $\mathbf{u}_l^\infty$ is the free-stream velocity, $\tilde{y}$ the distance along the wall from the starting point of the boundary layer, and $\Delta\delta$ the boundary mesh size. Equation [22] will be used in Section III–A to determine the necessary $\Delta\delta$ for adequate resolution of the wall boundary layers.

FLUENT™ formulation is fully implicit. Theoretically, there is no stability criterion that needs to be met in determining Δt. However, the time-steps used impact the accuracy, and hence the reliability, of the numerical results, especially for modeling transient phenomena. Due to the complexity of the coupling, there is no formulation to determine the optimal Δt. It must be determined empirically by test simulations. In the program, however, an automatic Δt controller is integrated. An initial time-step (*e.g.*, $\Delta t = 1 \times 10^{-3}$ s) is given. If more than 40 iterations are needed to meet the convergence criterion, the program will reduce Δt. If in less than 20 iterations converge is met, then a larger Δt is used.

A characteristic of the presented model is that h_l, h_s, c_l, c_s, f_l, p, n, $\mathbf{u}_l$, and $\mathbf{u}_s$ are coupled with each other *via* the auxiliary quantities d_s, μ_s, the exchange and source terms M_{ls}, U_{ls}, C_{ls}, Q_{ls}, and N, *etc.* A consequence of this coupling is, for example, that changing the momentum exchange model (Eq. [20]) affects the velocity fields of both liquid

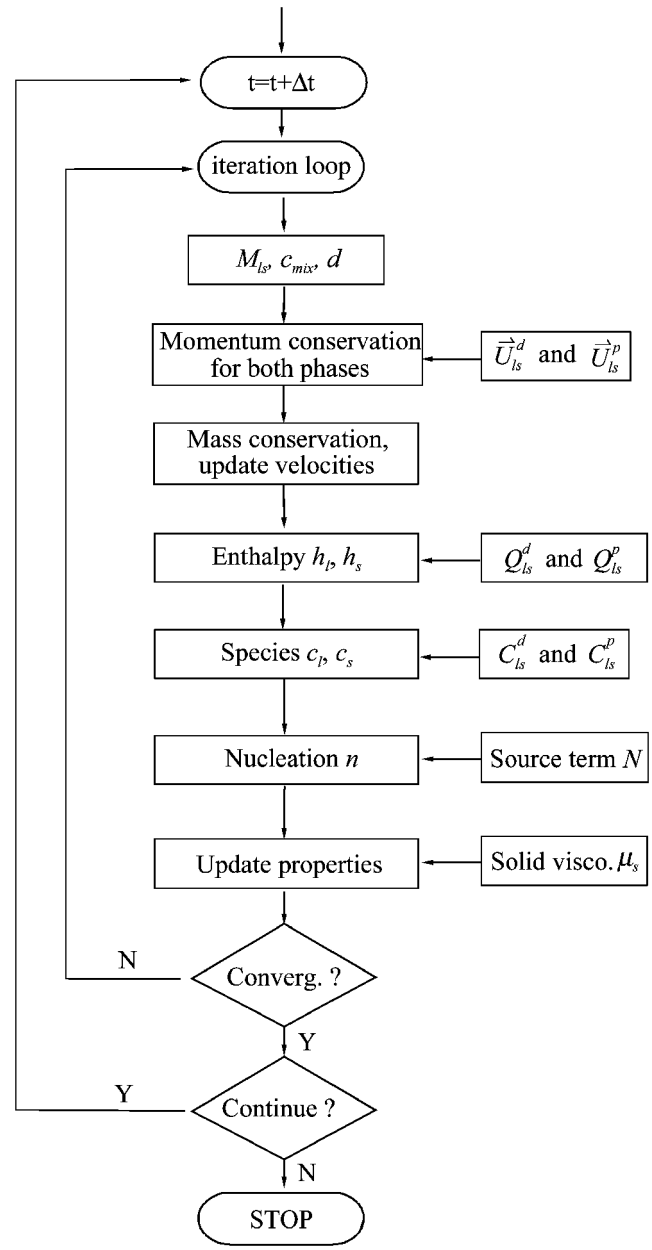

Fig. 2—Flow chart of the solution procedure by using FLUENT. Exchange and source terms, auxiliary quantities, and the user-defined conservation equation (nucleation and grain transport) are defined in user-defined subroutines, which are combined in the main software.

and solid. However, a change in the velocity fields will have an impact on the temperature and the concentration distributions. These two quantities estimate the mass transfer and the nucleation rate, which themselves affect the solid volume fraction and grain density. On the other hand, the solid volume fraction and grain density define the grain size, which, in turn, affects momentum exchange. Our model contains many of such circular arguments. However, some model details may be very important for the final results, such as macrosegregation pattern or grain size distribution, but others may not. Studying the relative importance of different model details on specific model predictions will be one of the importance issues of such a numerical model.

III. SIMULATION OF AN INGOT CASTING

A. *Description of the Studied Case*

In order to demonstrate the abilities of the present model, we consider the two-dimensional ingot casting shown in Figure 3. According to Eq. [22], the mesh must be fine enough to ensure the calculation accuracy. With the maximal velocity of 0.03 m/s in the casting and $\tilde{y}$ taken as the height of the casting (0.18 m), the mesh size $\Delta\delta$ adjacent to the wall must be less than 5.5 mm. In this study, the calculation

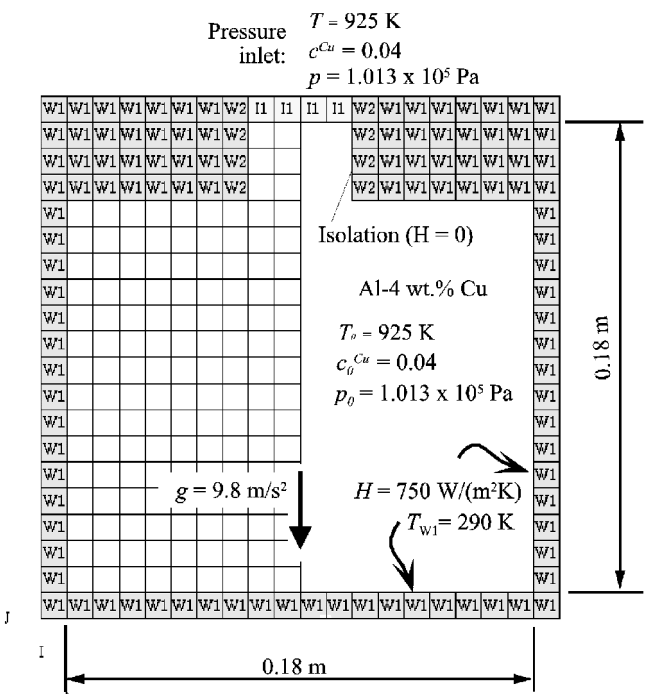

Fig. 3—Scheme of the studied case. For the simulations, we have used 40 × 40 square volume elements instead of the depicted 20 × 20. W1 represents the heat-transfer boundary elements with a coefficient of H = 750 W/(m^2 K) and a constant mold temperature of T_{w1} = 290 K. W2 represents the thermal isolation and I1 the pressure inlet.

domain is meshed into 40 × 40 square volume elements, The size of each element is 5 × 5 mm^2. The finer the volume elements, the smaller the time-step Δt necessary to meet the convergence criterion, and hence the higher the calculation cost. In the simulations presented subsequently, the automatic time-step controller is activated. In the initial stage of solidification, we have started with $\Delta t = 2 \times 10^{-4}$ s, while in the later stage, it is then automatically increased to 1×10^{-3} s. A single run of the simulation takes 2 weeks on a SGI Octane R12000 workstation (Silicon Graphics GmbH, Grasbrunn, Germany).

The casting is supposed to be filled instantaneously. Cooling starts from an initial temperature of 925 K. The surrounding mold (not modeled explicitly) is kept at a constant temperature of 290 K. A heat-transfer coefficient H at the casting/mold interface is introduced and assumed to be 750 W/(m^2 K). For both the liquid and the solid convection, we assume a nonslip boundary condition to be valid at the mold.

The recent model did not consider a free surface formed at the top of the casting. Therefore, we applied a special boundary condition with constant temperature, constant concentration, and constant pressure at I1 (pressure inlet) and considered the side wall of the inlet to be thermally isolated (Figure 3). Hot melt from the inlet I1 continuously feeds the solidification shrinkage.

We selected an inoculated A1-4 wt pct Cu alloy because of its almost globular equiaxed solidification morphology. Table I shows the physical properties and phase diagram parameters of this alloy. The densities of the liquid and solid are assumed to be constant but different, and therefore we do not take any thermal solutal convection into account. The parameters used for the nucleation law are $n_{\max} = 10^{14}$ m^{-3}, $\Delta T_N = 10$ K, and $\Delta T_\sigma = 4$ K. As for the mass-transfer rate, M_{ls}, it is necessary to know the grain diameter d_s; we assume an initial grain diameter of $d_s = 1$ μm and $g_\alpha = 5 \cdot 10^{-4}$ m/s.

B. *Results and Discussions*

Figure 4 shows the simulation results 8.0 seconds after the start of the cooling. In the initial stage both the isotherm and solidification isoline are symmetrical, and the solidification process is dominated by heat extraction of the mold. As soon as T drops below the liquidus, nucleation ($N > 0$) and solidification ($M_{ls} > 0$) start, first in the four corners, and subsequently along the mold walls. The solid forming directly on the wall does not move. The first reason for this is the applied non-slip boundary condition: the grains that nucleate on the surface are supposed to adhere to the wall. The second reason is that the local solidification rate at the surface and the corner regions is so high that a rigid shell (the fraction solid reaches the packing limit) forms in about 10 seconds. With the increasing f_s in the corners the melt becomes enriched in solute c_l. Although both f_s and n are

Table I. Thermophysical and Thermodynamic Properties Used in the Simulation

$\rho_l = 2606$ kg/m	$c_{p(l)} = 1179$ J/kg/K	$\mu_l = 1.3 \times 10^{-2}$ kg/m/s
$\rho_s = 2743$ kg/m	$c_{p(s)} = 766$ J/kg/K	$T_f = 933.5$ K
$k_l = 77$ W/m/K	$D_l^{Cu} = 5 \times 10^{-9}$ m^2/s	$k = 0.145$
$k_s = 153$ W/m/K	$D_s^{Cu} = 8 \times 10^{-13}$ m^2/s	$m = -344$ K

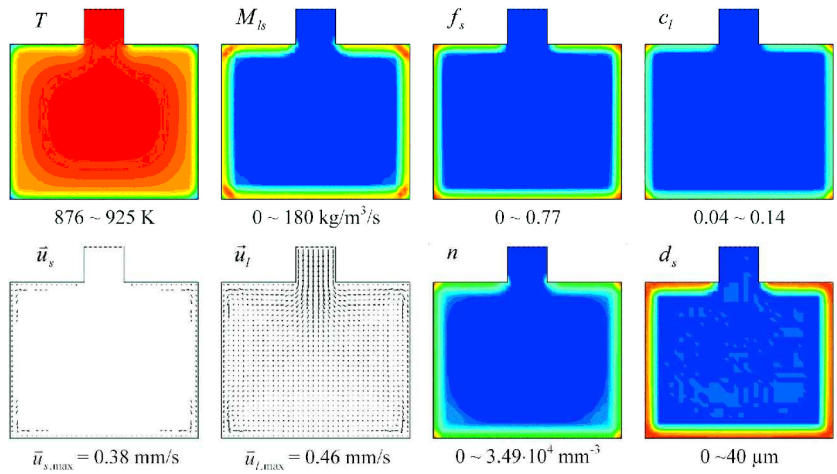

Fig. 4—Results of a simulation 8.0 s after cooling has started. The arrows of both velocity fields are continuously scaled starting from zero to the maximum value. All other quantities are scaled equidistantly by 30 colors, with blue representing the lowest and red the highest value. The minimum and maximum values are given below the corresponding picture.

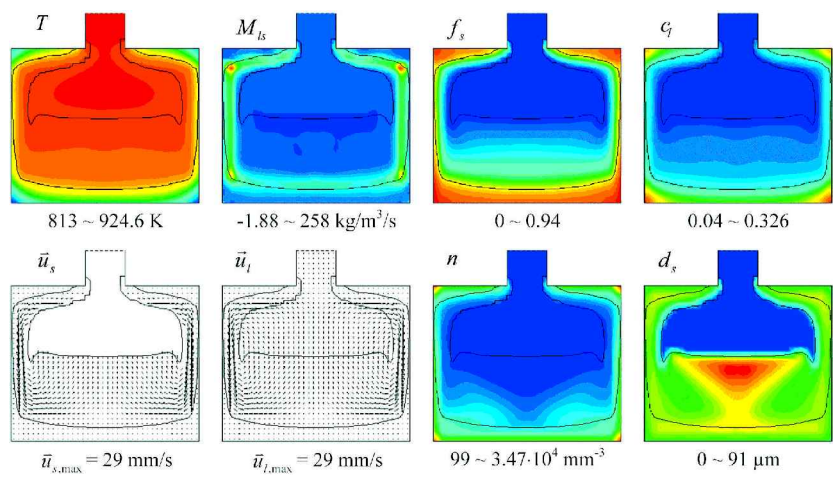

Fig. 5—Results of a simulation 35 s after cooling has started. The arrows of both velocity fields are continuously scaled starting from zero to the maximum value. All the other quantities are scaled equidistantly by 30 colors, with blue representing the lowest and red the highest value. The minimum and the maximum values are given below the corresponding picture. Two fraction solid isolines (0.01 and 0.64) are drawn together with each figure.

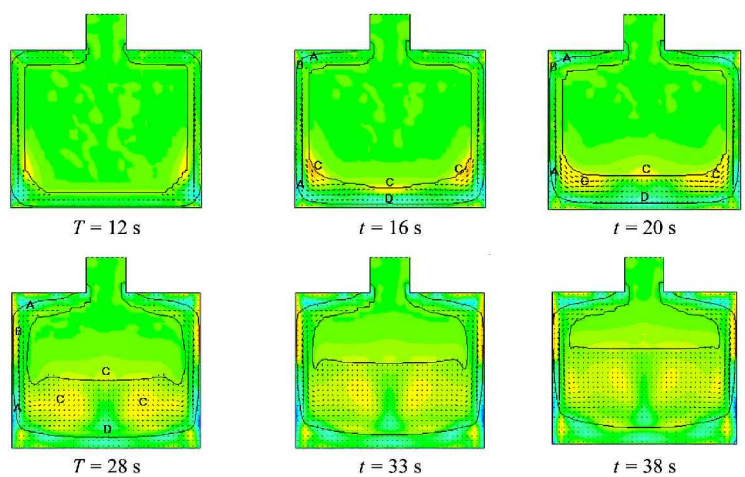

Fig. 6—Sequence of macrosegregation pattern (c_{mix}) overlaid with the velocity of the solid phase. The arrows of each velocity field are continuously scaled starting from zero to the maximum value. The value of c_{mix} is scaled with 30 colors, with blue representing the lowest (3.7 pct) and yellow the highest value (4.3 pct). Two fraction solid isolines (0.01 and 0.64) are drawn together with each figure.

much higher in the corners compared to areas along the mold walls, the average grain diameter is relatively uniform at the casting surface region. This is not surprising because the grain size is proportional to the cubic root of the ratio f_s/n and the higher fraction solid regions correspond to the higher grain density regions. The grain sedimentation and the sedimentation-caused convection in the initial stage are not significant, but the feeding flow is strong. This feeding flow is caused by solidification shrinkage and depends on the integrated mass-transfer rate.

With further solidification, those solid grains, which are not directly adhered to mold wall sink downward. Figure 5 shows the simulation results after 35 seconds. Because the solid and liquid are coupled through the momentum exchange terms, the melt is drawn by the sinking solid. Two vortices occur in the bulk melt—one clockwise in the right half and one counterclockwise in the left half of the casting. The packing limit is exceeded in the four corner regions and the packing solid forms a rigid porous body there. Sedimentation leads to the accumulation of solid mainly at the bottom corners, but also along the bottom itself. Due to this sedimentation, the f_s isolines at the lower bottom regions proceed faster than in the side wall regions. For $f_s < f_s^c = 0.637$ (packing limit), the solid and liquid move in a similar manner along the two vortices. The flow currents become so strong that they carry the solid upward toward the hot center of the casting, causing the solid to melt (dark blue area in the M_{ls} distribution: $M_{ls} < 0$). According to Eq. [18], remelting can only occur if $\Delta T = T_f + m \cdot c_l - T < 0$. There are two parameters contributing to the negative ΔT, the temperature and solute enrichment in the casting center. Compared to Figure 4, the grain density in the corner regions and along the mold walls remains almost unchanged. However, new grains nucleate in the bulk melt. As soon as the grains nucleate, they quickly grow to an average size of around 50 μm, the largest in the middle bottom region, where the solid volume fraction is between 0.3 and 0.5.

Figure 6 shows the complexity of macrosegregation formation. Different segregation regions are marked with A through D. First segregations appear in the lower corner regions 10 seconds after the cooling has started. The negative segregations A ($c_{mix} < 4$ pct) are caused by the sedimentation. The solute poor grains sink along the wall and settle there as the local fraction solid exceeds the packing limit $f_s^c = 0.637$. According to Eq. [13], the mixed concentration c_{mix} is determined by α_s, α_l, c_l, and c_s. As c_s is much lower than the c_l, regions with higher grain settlement rate have lower mixed concentration c_{mix}. The positive segregation zone C just close to A at the lower corner is caused by melt flow. As the grains settle in zone A, solute-enriched melt has to leave this region in order to provide space for the settling grains. This solute-enriched melt is removed from region A by the convection so that the positive segregation zone C is just near to it. This positive segregation forms temporally in the bulk melt and will move with the melt flow while solidification proceeds.

Similarly negative segregations A form near the top corners. Again, grain sedimentation is the origin of their formation. The $\mathbf{u}_s$ field shows that the grains nucleated near the upper wall tend to move toward the corner. The grains moving toward the corner cause the local fraction solid to increase. As f_s exceeds the packing limit, $\mathbf{u}_s$ vanishes and the oncoming grains settle here and hence negative segregations form. However, in the late stage of solidification, these negative segregated zones A move gradually downward. As the local f_s exceeds the packing limit, the oncoming grains settle and broaden the negative segregation zones, while the melt penetrates through the voids between the packed grains to feed the solidification shrinkage. The solute-enriched feeding melt can partially level out the negative segregation near the casting wall so that the negative segregation becomes weaker.

The positive segregation area B just below the upper corners is also produced by grain movement. A gradient in solid velocity is present in front of zones B (Figure 6). The grains at the corner cannot move. However, just below the corner, when the local fraction solid is still smaller than the packing limit, the grains start to sink. Thus, grains can leave the region B before the packing limit is exceeded. The volume of the exiting grains must be filled by the solute-enriched melt. The direct outcome of this phase transport phenomenon, *i.e.*, the exit of the solute poor solid and the feeding by the solute-enriched melt, is the increase of the local mixed concentration c_{mix}.

At $t = 16$ seconds, a negative segregated area D occurs on the lower bottom wall near the area of $f_s > f_s^c = 0.637$ caused again by the grain sedimentation. This lower concentration area D results in a corresponding higher concentration area C located directly at the outer boundary of the mushy zone. As solidification proceeds, the three higher concentration areas C located at the outer boundary of the mushy zone (labeled C in Figure 6) are not fixed. They move with the flow currents and ascend toward the inner regions of the casting.

Figure 7 shows the evolution of grain structure. According to the nucleation law,[1,17,28] applied in this model, the undercooling $\Delta T = T_f + m \cdot c_l - T$ is the only driving force for nucleation. If grain movement is disregarded, the local grain density will be determined by the maximum ΔT. The maximum ΔT achieved in the surface region and at the corner is 6 to 8 K, which is much higher than the maximum ΔT achieved in the bulk melt region (<1 K). Because the grain movement in the corner and surface regions is negligible, the maximum grain density at the corner and surface regions will remain unchanged on further solidification. Both nucleation and grain movement produce a V-shaped isoline of n in the lower region after about 30 seconds. As solidification progresses, new grains nucleate continuously in the bulk melt near the zero f_s isoline. In the meantime, the grains that are nucleated near the upper corner or along the vertical wall regions are transported according to the present solid velocity. Therefore, grain densities in the lower regions increase and the V shape of the n isolines is transformed gradually.

As already discussed, although we predict high grain densities along the casting walls, the grain size distribution is relatively uniform (~50 μm). At about 30 seconds, relative large grains appear near the lower center region. The solid velocity field indicates that the large grains may have been transported from the upper regions. The grains nucleated along the vertical wall sink and grow as they move. When they reach the lower center region, they have grown to a relatively large extent. As solidification proceeds, the large

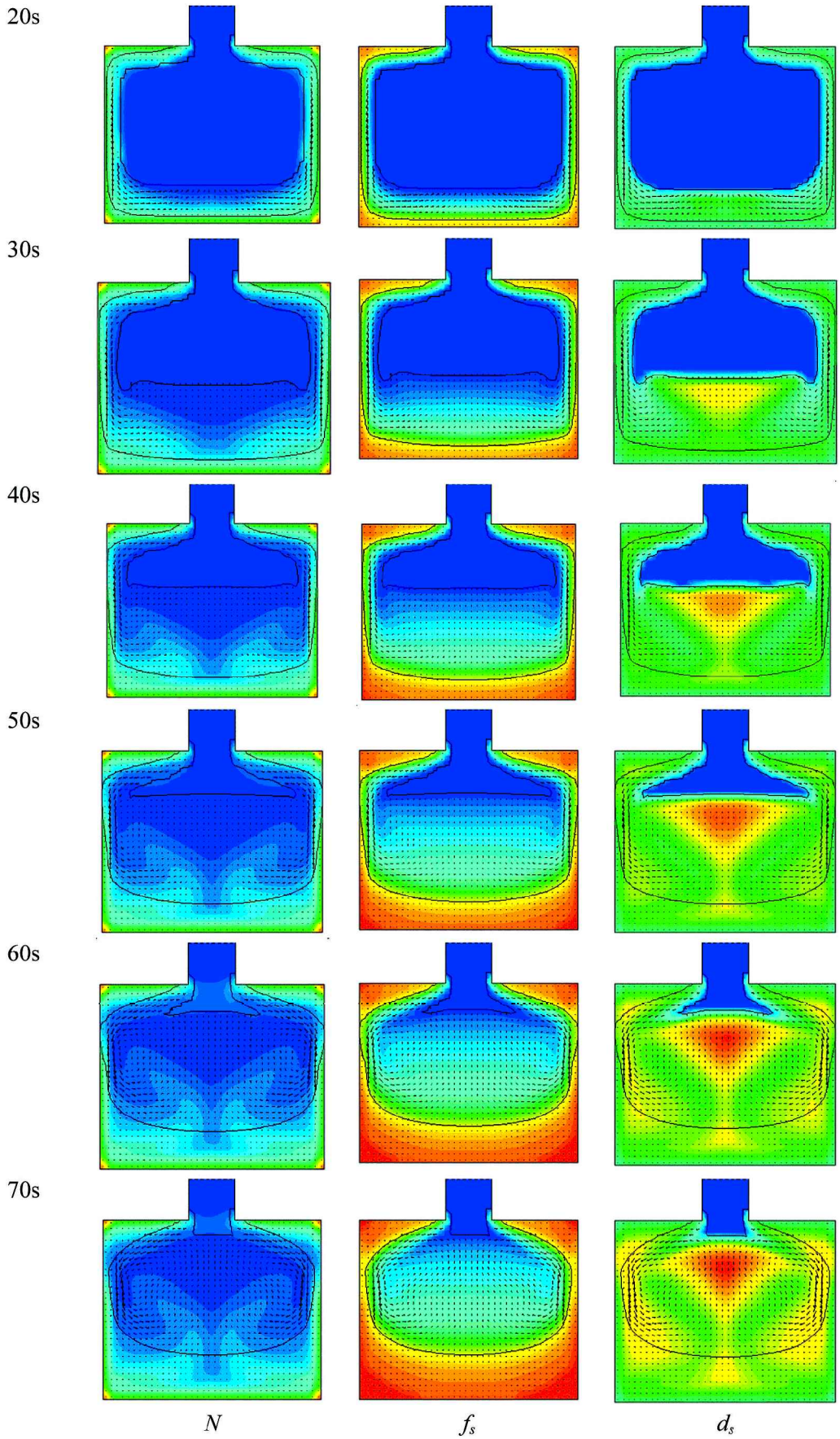

Fig. 7—Sequence of grain evolution. All the quantities are equally scaled with 30 colors, with blue representing the lowest and red the highest value. The grain density is scaled from 0 to $3.47 \cdot 10^4$ mm^{-3}, the fraction solid 0 to 0.99, and the grain diameter 0 to 115 μm. The solid velocity field is also shown together with the grain density. Two fraction solid isolines (0.01 and 0.64) are drawn together with each figure.

grain zone moves upward according to solid velocity. The grains continue to grow and to move.

C. *Reliability Analysis and Future Works*

As mentioned in Section II–A, the recent model is valid for laminar flow. According to the simulation results, the maximum velocity achieved in the casting is 0.03 m/s. The character size L (casting size) in this case study takes 0.18 m. The system Reynolds number $\mathrm{Re} = D \cdot \mathbf{u}_l \cdot \rho_l/\mu_l$ is thus about 1080, less than the critical number 2100, so the assumption of laminar flow in this case is justified. The microdrag force model used (Eq. [20]) is also based on the assumption of laminar flow. Due to the strong coupling between the two phases, the relative velocity $\Delta\mathbf{u} = |\mathbf{u}_l - \mathbf{u}_s|$ between the solid and the liquid is very small. Therefore, we find that the Reynolds number for two-phase flow $\mathrm{Re} = d_s \cdot \rho_l \cdot f_l \cdot \Delta\mathbf{u}/(\mu_l \cdot f_s)$ is much smaller than the critical number of 10.

The mesh size is an important factor influencing the calculation accuracy. Fine mesh improves the accuracy, but increases the calculation time. In the present article, the mesh size at the wall must be smaller than the one described by the criterion (Eq. [22]). This mesh criterion ensures that the velocity gradient at the wall is adequately approximated by the difference expression. For future work, it is necessary to reduce the calculation time by considering the sophisticated numerical technique, *e.g.*, parallel computing and unstructured meshes.

The recent simulation results have not yet been compared with the experiments. Before doing so, the following points need to be further considered in the model.

(1) The recent model cannot handle the free surface and concentrated shrinkage pores (cavities), which may form at the casting top or in the casting center due to the solidification shrinkage. Therefore, an ideal boundary condition at the casting top, *i.e.*, pressure inlet, is applied. Hot melt can flow through this inlet to feed the casting continuously. However, with this boundary condition, the casting can never completely solidify.
(2) Only sedimentation-induced flow and feeding flow are considered here and the thermosolutal convection is ignored. The thermosolutal convection would influence the general flow pattern and, consequently, the macrosegregation distribution.
(3) The parameters used for the nucleation law and grain growth are critical for the calculation of the grain density and grain diameter. Experimental casting trials for the investigated alloy and statistical analyses[1,17] must be undertaken to determine those parameters.

Despite the simplifications, the recent numerical model provides an effective method to study the globular equiaxed solidification process. Some hypotheses and theories were achieved in the last decades for the explanation of macrostructure and macrosegregation formation;[31,32] however, it is difficult to use those theories to explain the results in the real castings, because the complicated nucleation and grain growth processes, convection, grain movement, solute transportation, *etc.*, are not so easily observed. The numerical model offers the possibility to "visualize" all those details.

IV. CONCLUSIONS

The presented model is able to simulate globular equiaxed solidification including nucleation, grain evolution, melt convection, sedimentation, solute transport, and macrosegregation formation. It is an effective method of coupling the macroscopic solidification processes with microscopic phenomena. By analyzing the simulation results for the solidification of an Al-4 wt pct Cu ingot casting, a deep understanding of the following features could be achieved.

1. Due to heat extraction, grains initially nucleate in the vicinity of the mold wall. As their density is higher than the surrounding melt, those grains with no direct contact to the mold wall start to sink.
2. The sinking of grains produces a downward melt flow along the mold wall and a corresponding upward flow in the middle of the casting.
3. Sinking grains partly settle at the bottom of the casting and partly flow with the melt current into the bulk melt. Here, remelting occurs. However, we did not predict any grain dissolution.
4. Grain settlement always results in negative macrosegregation. We predict grain settlement (a) in the upper corners, (b) at the bottom of vertical walls, and (c) at the bottom in the middle of the casting.
5. Positive macrosegregation may form for two reasons: (1) depletion of grains and the corresponding inward flow with segregated melt and (2) squeezing out of segregated melt by settling grains. Areas of positive macrosegregation caused by the latter are mainly liquid and thus may move during the course of solidification. Those caused by the former do not move.
6. Feeding flow with segregated melt into areas with large solid fraction reduces negative and increases positive macrosegregation.
7. Grains that form in contact with the mold wall do reveal their final small size directly at the beginning of the solidification process. Moving grains generally grow during motion. Those grains that are transported into the bulk melt and do not melt grow the most. Therefore, an area of large grains is typically located in the center of the casting.

NOMENCLATURE

c_0	initial concentration
c_l, c_s	species concentration
c^*	interface species
$C_{ls}(= -C_{sl})$	species exchange rate
$C^d_{ls}(= -C^d_{sl})$	species diffusional flux
$C^p_{ls}(= -C^p_{sl})$	species exchange due to phase change
c_{mix}	mix concentration
$c_{p\,(l)}$, $c_{p\,(s)}$	specific heat
D_l, D_s	diffusion coefficient
d_s	grain diameter
f_l, f_s	volume fraction
f^c_s	grain packing limit
$\mathbf{g}$	gravity
g_α	growth factor
H	heat-transfer coefficient
H^*	heat-transfer coefficient at the *s*/*l* interface
h_l, h_s	enthalpy

h^*	interface enthalpy
Δh_f	latent heat (heat of fusion)
K	permeability of liquid in porous medium
$K_{sl}(= K_{ls})$	momentum exchange coefficient
k	distribution coefficient of phase diagram
k_l, k_s	thermal conductivity
L	character size of the fluid domain
$M_{ls}(= -M_{sl})$	mass-transfer rate
M	slope of liquidus in phase diagram
N	grain production rate
n	grain density
$n_{\max}$	maximum grain density
p	pressure
p_0	initial pressure
$Q_{ls}(= -Q_{sl})$	energy exchange rate
$Q^d_{ls}(= -Q^d_{sl})$	energy exchange by heat transfer
$Q^p_{ls}(= -Q^p_{sl})$	energy change due to phase change
T_0	initial temperature
T, T_l, T_s	temperature
T_E	eutectic temperature
T_f	melting point of pure metal (Al)
T_{wl}	boundary temperature
T_{ref}	reference temperature for enthalpy definition
ΔT	undercooling
ΔT_N	Gaussian distribution width of nucleation law
ΔT_σ	undercooling for maximum grain production rate
t	time
$\mathbf{U}_{ls}(= -\mathbf{U}_{sl})$	momentum exchange rate
$\mathbf{U}^d_{ls}(= -\mathbf{U}^d_{sl})$	momentum change due to drag force
$\mathbf{U}^p_{ls}(= -\mathbf{U}^p_{sl})$	momentum exchange due to phase change
u_l, u_s	velocity component in x direction
$\mathbf{u}_l$, $\mathbf{u}_s$	velocity vector
$\mathbf{u}_{ls}$, $\mathbf{u}_{sl}$	interphase velocity
$\mathbf{u}^*$	interface velocity
$\Delta\mathbf{u}$	relative velocity between two phases
v_l, v_s	velocity component in y direction
$\mathbf{y}$	length of boundary layer
$\Delta\delta$	boundary mesh size
ρ_l, ρ_s	density
μ_l, μ_s	viscosity
μ_{mix}	mix viscosity
$\bar{\bar{\tau}}_l$, $\bar{\bar{\tau}}_s$	stress-strain tensors

Note: The subscripts l and s mark the liquid and solid phases, respectively.

ACKNOWLEDGMENTS

Financial support for this research has been provided by the German Science Foundation (DFG) as part of the collaborative research centers SFB 370 and SFB 289. The authors also acknowledge the excellent technical assistance of Dr. S. Pelzer and Dr. M. Braun, FLUENT (Darmstadt, Germany).

REFERENCES

1. M. Rappaz: *Int. Mater. Rev.*, 1989, vol. 34, pp. 93-123.
2. C. Beckermann and R. Viskanta: *Appl. Mech. Rev.*, 1993, vol. 46, pp. 1-27.
3. J. Ni and C. Beckermann: *Metall. Trans. B*, 1991, vol. 22B, pp. 349-61.
4. C.Y. Wang and C. Beckermann: *Metall. Mater. Trans. A*, 1996, vol. 27A, pp. 2754-64.
5. C.Y. Wang and C. Beckermann: *Metall. Mater. Trans. A*, 1996, vol. 27A, pp. 2765-83.
6. C.Y. Wang and C. Beckermann: *Metall. Mater. Trans. A*, 1996, vol. 27A, pp. 2784-95.
7. C. Beckermann: *JOM*, 1997, vol. 49, pp. 13-17.
8. A.V. Reddy and C. Beckermann: *Metall. Mater. Trans. B*, 1997, vol. 28B, pp. 479-89.
9. J. Ni and F.P. Incropera: *Int. J. Heat Mass Transfer*, 1995, vol. 38, pp. 1271-84.
10. J. Ni and F.P. Incropera: *Int. J. Heat Mass Transfer*, 1995, vol. 38, pp. 1285-96.
11. O. Nielsen, A. Appolaire, H. Combeau, and A. Mo: *Metall. Mater. Trans. A*, 2001, vol. 32A, pp. 2049-60.
12. M.C. Flemings: *Proc. 3rd Int. Conf. on Semi-Solid Processing of Alloys and Composites*, Tokyo, June 1994, pp. 3-6.
13. D. Ghosh, R. Fan, and C. Van Schilt: *Proc. 3rd Int. Conf. on Semi-Solid Processing of Alloys and Composites*, Tokyo, June 1994, pp. 85-94.
14. A. Ludwig, G. Ehlen, M. Pelzer, and P.R. Sahm PR: *Proc. MCWASP IX, SIM2000*, Shaker-Verlag, Aachen, pp. 175-82.
15. A. Ludwig, M. Wu, G. Ehlen, and P.R. Sahm: *Materials Week 2000*, Munich, Germany, Sept. 25–28, 2000.
16. W. Kurz and D.J. Fisher: *Fundamentals of Solidification*, Trans Tech Publications, Aedemannsdorf, Switzerland, 1989.
17. P. Thevoz, J.L. Desbiolles, and M. Rappaz: *Metall. Trans. A*, 1989, vol. 20A, pp. 311-22.
18. M. Ishii and N. Zuber: *AIChE J.*, 1979, vol. 25, pp. 843-55.
19. C.Y. Wang, S. Ahuja, C. Beckermann, and H.C. de Groh III: *Metall. Trans. B*, 1995, vol. 26B, pp. 111-19.
20. M.K. Denison and B.W. Webb: *J. Heat Transfer*, 1993, vol. 115, pp. 1002-12.
21. D. Gidaspow, L. Chungliang, and Y.C. Seo: *Ind. Eng. Chem. Fundam.*, 1983, vol. 22, pp. 187-93.
22. D. Gidaspow and B. Ettehadieh: *Ind. Eng. Chem. Fundam.*, 1983, vol. 22, pp. 193-201.
23. R.A.W.M. Henkes and C.J. Hoogendoorn: *Trans. ASME*, 1994, vol. 116, pp. 400-08.
24. S. Acharya and F.H. Moukalled: *Num. Heat Transfer B*, 1989, vol. 15 (2), pp. 131-52.
25. J.O. Hinze: *Turbulence*, McGraw-Hill Publishing Co., New York, NY, 1975.
26. C.T. Bowman: in *Fossil Fuel Combustion*, W. Bartok and A.F. Sarofim, eds., John Wiley & Sons, Toronto, Canada, 1991.
27. R.B. Bird, W.E. Stewart, and E.N. Lightfoot: *Transport Phenomena*, John Wiley & Sons, New York, NY, 1960.
28. W. Oldfield: *Trans. ASM*, 1966, vol. 59, pp. 945-61.
29. S.V. Patankar: *Numerical Heat Transfer and Fluid Flow*, Hemisphere Publishing Corp., Washington, DC, 1980.
30. H. Schlichting: *Boundary-Layer Theory*, McGraw-Hill Publishing Co., New York, NY, 1979.
31. J. Campbell: *Castings*, Butterworth Heinemann Ltd. Oxford, United Kingdom, 1991.
32. A. Ohno: *Solidification—The Separation Theory and Its Practical Applications*, Springer-Verlag, Berlin, 1987.